ADVANCED MATERIALS TECHNOLOGIES
www.advmattechnol.de

Ultra-Broadband Metamaterial Absorber Based on Multilayer Resistive Film Frequency Selective Surface

*Yue Wang, Mengzhen Yang, Tianze Li, Xinkai Qi, Jun Wang, Shiyin Li, and Lei Zhao**

In this paper, an ultra-broadband metamaterial absorber is proposed based on multilayer resistive film frequency selective surface (RFSS). Each dielectric-resistive layer consists of polymethacryimide (PET) and resistive film, achieving effective absorption through multilayer loss. Both strip-shaped and square-shaped resistance film layers exhibit significant symmetry. Simulated results reveal that the −10 dB operating bandwidth of metamaterial absorber (MMA) is from 1.07 to 11.84 GHz with a fractional bandwidth of 166% and a thickness of only 0.105 λ_L. It covers the L-, S-, C-, and X-bands with strong low-frequency absorption to broaden the bandwidth. The equivalent circuit model is established based on Costa's model, serving as the theoretical analysis. Accurate models for each resistive film surface configuration are derived, modeling the resistive film surface as a series RLC circuit. Additionally, the designed metamaterial absorber is fabricated and measured in microwave anechoic chamber, and the measurement results are generally consistent with the simulated ones, further validating the effectiveness of the design.

1. Introduction

Metamaterial absorbers (MMAs)[1,2] are widely used because they can effectively attenuate electromagnetic waves in the target frequency range. Recently, frequency selective surface (FSS)[3,4] as an effective structure for controlling electromagnetic waves has received extensive attention.

Traditional metamaterial absorbers typically consist of a metallic surface layer, dielectric and metal grounded layers. The Salisbury screen[5,6] consisted of lossless dielectric spacer with a resistive screen. The thickness of spacer was ≈1/4 wavelength and placed in front of the metal ground layer. Jang et al.[7] presented an optically transparent and polarization-independent microwave absorber by using Al wire gird to construct the bow-tie array to induce high ohmic loss, which achieved an absorption coefficient more than 90% from 5.8 to 12.2 GHz. Although the structures effectively have reduced the intensity of electromagnetic waves within specific frequency band, the absorption bandwidth was narrow and could not achieve more excellent broadband absorption. To overcome bandwidth limitations, researchers have introduced multilayer designs. For example, the Jaumann absorber[8] broadened the bandwidth by using additional layers. However, this multilayer approach often increases thickness. Consequently, a trade-off remains between achieving broadband absorption and minimizing thickness.

The microwave band is widely used in the fields of radar, satellite communications, and wireless broadcasting, etc, so the research of MMA applied within this band is of great significance. To achieve broadband absorption and lower thickness of MMA, researchers have further explored innovative solutions by combining resistive films with FSS.[9,10] By replacing the metallic layer in FSS with resistive film, the electromagnetic loss characteristics can be improved, leading to better bandwidth, wide-angle performance, and stability. For example, a multilayer absorber has been demonstrated using an equivalent circuit model (ECM), achieving a −10 dB bandwidth of 176.2% with a thickness of 0.098λ_L, where λ_L refers to the wavelength corresponding to the lowest operating frequency.[11] Similarly, an absorber with a square-loop array and lumped resistors has been introduced,[12] significantly increasing bandwidth. These results have highlighted the application of impedance matching and loss optimization in broadband absorbers. Lan H. W. et al.[13] further showed that combining resistive film with FSS can achieve more than 90% absorption across the 1.91–20.78 GHz range with a thickness of 0.102 λ_L. Zheng et al.[14] designed an MMA using three different structures of resistive film patch arrays, which is capable of achieving an absorption coefficient more than 90% from 2.2 to 18 GHz with a fractional bandwidth of ≈156.4%. Li et al.[15] proposed a transparent ultra-wideband double-resonance-layer absorber by using resistive films as frequency selective surfaces, which can achieve ultrawide microwave absorption in the range of 2.00 to 11.37 GHz with a fractional bandwidth of 140.2%.

Y. Wang, M. Yang, T. Li, X. Qi, J. Wang, S. Li, L. Zhao
School of Information and Control Engineering
China University of Mining and Technology
Xuzhou 221116, China
E-mail: leizhao@cumt.edu.cn
Y. Wang
School of Safety Engineering
China University of Mining and Technology
Xuzhou 221116, China
Y. Wang
Yuyao Sunny Intelligent Optical Technology Co., Ltd
Ningbo 315400, China

The ORCID identification number(s) for the author(s) of this article can be found under https://doi.org/10.1002/admt.202500785

DOI: 10.1002/admt.202500785

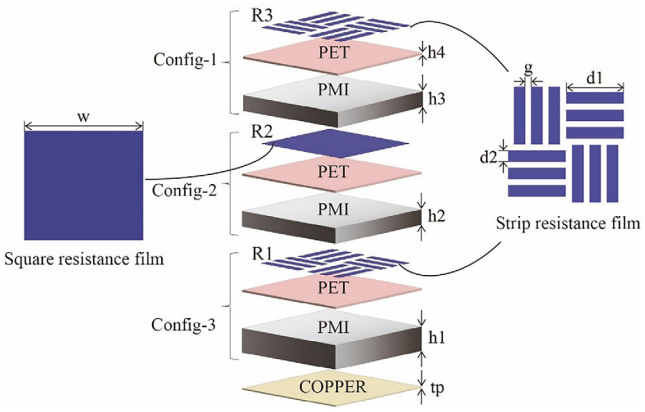

Figure 1. 3-D schematic of the proposed absorber's unit cell structure.

In this paper, an ultra-broadband metamaterial absorber based on a multilayer resistive film frequency selective surface (RFSS) is proposed. The proposed design creatively combines resistive films with FSS and employs a detailed circuit model analysis of the resistive film layer, which effectively enhances low-frequency absorption and broadens the absorption bandwidth. The absorber achieves a reflection coefficient continuously below −10 dB across the 1.07–11.84 GHz band, with a thickness of only 0.105 λ_L.

2. Design Consideration

2.1. Unit Cell Structure of the Absorber

Figure 1 shows the 3-D schematic unit cell of the proposed absorber, which comprises Config-1, Config-2, Config-3, and a copper grounded plane. Each configuration consists of a polymethacryimide (PET) layer, a polymethacryimide (PMI) layer, and a resistive film layer. The resistive film layer is printed in periodic arrangement on the PET substrate with $\epsilon = 3.0$, $\tan\delta = 0.061$ and the thickness of h_4, which has good stability of dielectric constant and loss factor, visible light transmittance and flexibility to improve mechanical stability and conformability. Each layer is separated by a PMI foam ($\epsilon = 1.05$, $\tan\delta = 0.00$l) with thickness of h_1, h_2, and h_3, which functions as a lightweight spacer to reduce interference. The unit cell's period is denoted as p. The parameters are (mm): $p = 20$, $t_p = 0.018$, $h_1 = 14$, $h_2 = 7$, $h_3 = 8$, $h_4 = 0.175$, $d_1 = 10$, $d_2 = 2$, $g = 1$, $w = 19.4$.

2.2. Equivalent Circuit Model (ECM) Analysis of the Proposed Absorber

The electromagnetic response of the absorbing structure in different frequency bands can be mapped as a set of series or parallel *RLC* resonant circuits, and the EMC composed of these circuits can effectively capture the broadband absorption characteristics of the absorber. To accurately derive the ECM of the proposed absorber, each resistive film frequency-selective surface (RFSS) configuration was analyzed first based on Costa's ECM,[16–19] as shown in **Figure 2**.

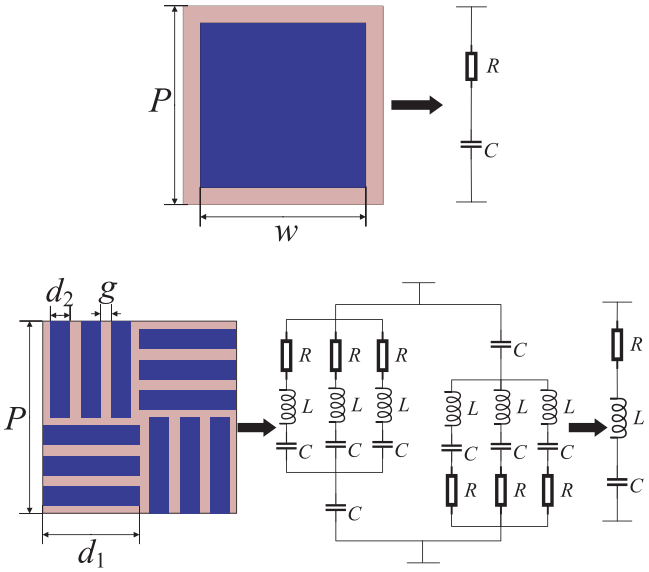

Figure 2. The ECM of the square and strip resistance film.

Assuming a vertical electric field orientation, *C* represents the equivalent capacitance for gaps between different strips, while *L* and *R* represent the series equivalents for the strips themselves. The square patch FSS exhibits a capacitive, and the inductance can be negligible because the electric field is perpendicular to the patch and no significant current loops are formed at low microwave frequencies. Therefore, the inductance is substituted by a short circuit, which simplifies the *RLC* series circuit to an *RC* series circuit. Therefore, the square resistance film (RFSS2) is equivalent to an *RC* series circuit. For the single strip resistive film FSS, the longer strip forms current loops that introduce inductance (*L*) into the circuit. Thus, the single strip resistive film FSS is equivalent to an *RLC* series circuit. Similarly, the strip resistive films (RFSS1, RFSS3) are initially equivalent to three *RLC* series circuits in parallel, with each strip creating its own inductance and capacitance. These three parallel *RLC* series circuits are then connected in series with a capacitor (as the strips are oriented perpendicular to the electric field), and subsequently in parallel with another identical circuit that has a symmetrical structure. Ultimately, the entire configuration of RFSS1 and RFSS3 is represented as an *RLC* series circuit. The resistance *R*, inductance *L* and capacitance *C* in the *RLC* circuit are closely related to the loss mechanism, electromagnetic coupling effect

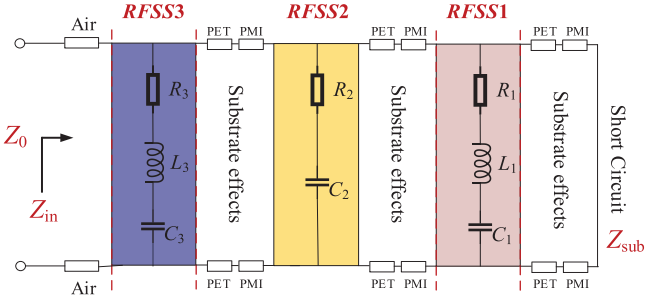

Figure 3. The ECM of the proposed MMA.

Table 1. Comparison of Theoretical and Optimized Values of *RLC*.

Component	R_1[Ω]	R_2[Ω]	R_3[Ω]	C_1[fF]	C_2[fF]	C_3[fF]	L_1[nH]	L_3[nH]
Theoretical Value	666.67	212.56	266.67	46.48	408	46.48	13.67	13.67
Optimized Value	666.67	212.56	266.67	46.48	520.5	30.2	13.67	13.67

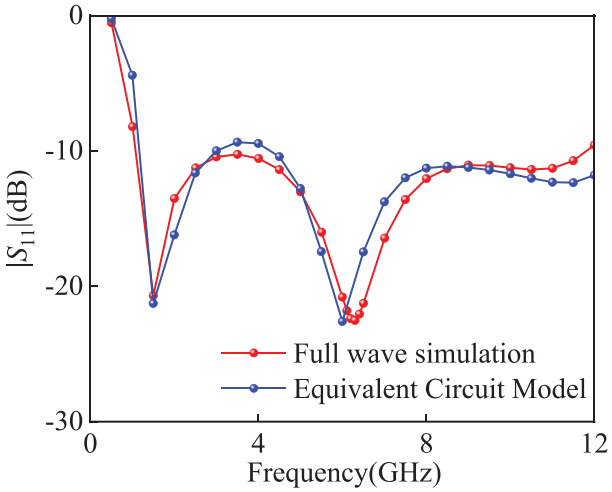

Figure 4. Comparison of $|S_{11}|$ curves from CST simulation and ADS optimization.

and structural resonance, and the circuit impedance can be regulated by adjusting their values to realize that the input impedance matches well with the free-space impedance (≈377 Ω) within operating band in order to achieve the minimum reflection. **Figure 3** shows the simplified ECM of the proposed MMA, based on the above ECM of the resistive film frequency-selective surface. The ECM of MMA consists of three key components: RFSS1, RFSS2, and RFSS3. Each RFSS layer is represented by its corresponding equivalent circuit elements, including resistances (R_1, R_2, and R_3), capacitances (C_1, C_2, and C_3) and inductances (L_1, L_3). By cascading the design of multiple series or parallel *RLC* resonant loops, multiple resonant peaks can be superimposed to form a continuous broadband absorption region. Especially at the band edge, the circuit generates an auxiliary resonance or transition response that can effectively enhance the absorption efficiency.

From Figure 3, the grounded substrate is represented by the short-circuited transmission line. Notably, the impedance of Z_{RFSS} is a pure real value, dominated by resistance, effectively dissipating electromagnetic energy. In contrast, the grounded substrate's impedance Z_{sub} is complex due to the imaginary component ($j\epsilon'_1$), reflecting its ability to store and release energy. This can be expressed using the relative permittivity $\epsilon_1 = \epsilon'_1 - j\epsilon''_1$, as expressed in the following Equation (1):[20]

$$Z_{sub} = Z_0 \cdot \sqrt{1/\epsilon_1} \cdot tanh\left\{j\left(2\pi fh/c\right) \cdot \sqrt{\epsilon_1}\right\} \tag{1}$$

where f presents the operating frequency, h is the absorber thickness, Z_0 is the air impedance, and c is the light speed.

To better match the input impedance of our absorber with free-space wave impedance, we introduced reactance components into Z_{RFSS}, as shown in Equation (2). The impedance of the RFSS can be expressed as a series-connected *RLC* circuit.

$$Z_{RFSS} = R - j\left(\frac{1-\omega^2 LC}{\omega C}\right) \tag{2}$$

where ω is the angular frequency, R, L, and C represent the equivalent resistance, inductance, and capacitance, respectively.

The reactive components, $Im(Z_{RFSS})$ of the resistive film frequency selective surface (RFSS) and $Im(Z_{sub})$ of the grounded dielectric slab are connected in parallel. $Im(Z_{in})$ can be expressed as Equation (3):

$$Im\ \left(Z_{in}\right) = \frac{Im\left(Z_{RFSS}\right) \cdot Im\left(Z_{sub}\right)}{Im\left(Z_{RFSS}\right) + Im\left(Z_{sub}\right)} \tag{3}$$

To further analyze the impedance behavior of the RFSS layers, we derived the individual equivalent circuit parameters for R, C, and L. The equivalent resistance R can be calculated as the following Equation (4):

$$R \approx R_S \cdot \frac{S}{A} \tag{4}$$

where R_S is the surface resistance, S is the surface area of a unit cell, and A is the surface area of the lossy element within a single unit cell.

The capacitance C is determined by the length of the line where charge accumulates at the edge of the resistive film and

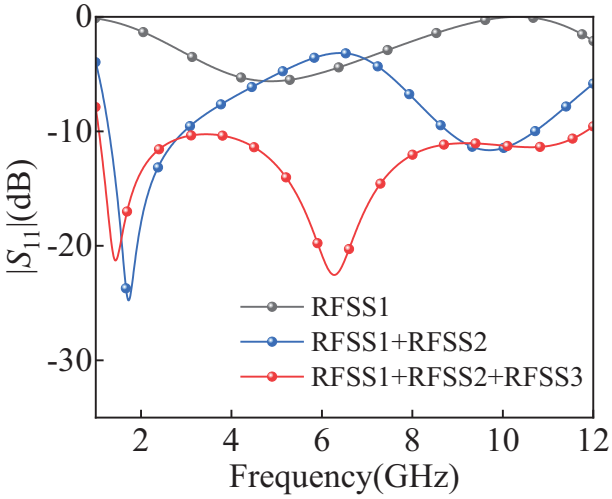

Figure 5. Absorption performance of absorbers with different layer configurations.

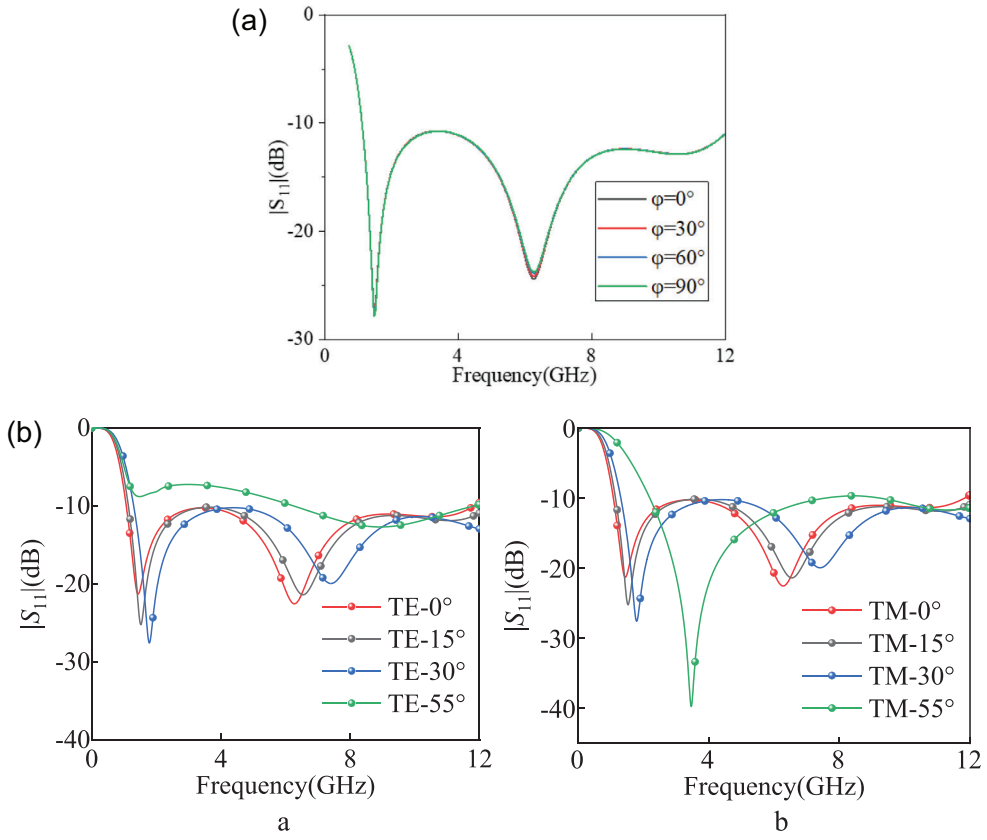

Figure 6. a) $|S_{11}|$ curves for different polarizing angles. b) $|S_{11}|$ curves for different incidence angles in (a) TE and (b) TM modes.

can be expressed using Equations (5) and (6) for an ideal parallel plate capacitor:[21,22]

$$C = \frac{\epsilon_0 \cdot \epsilon_r \cdot S}{d} \tag{5}$$

$$S = l \cdot d_R \tag{6}$$

Here, ϵ_0 denotes the vacuum permittivity, ϵ_r denotes the relative permittivity, S is the plate area of the capacitor, d is the plate spacing, and the thickness of the conductive patch $d_R = 0.175$ mm. These parameters determine the value of capacitance together.

At the same time, the inductance L is associated with the wire length carrying current across the resistive film surface, as shown in Equations (7) and (8):

$$L = \frac{\mu_0 \cdot \mu_r \cdot l}{\pi \cdot ln\left(d_i \cdot l\right)} \tag{7}$$

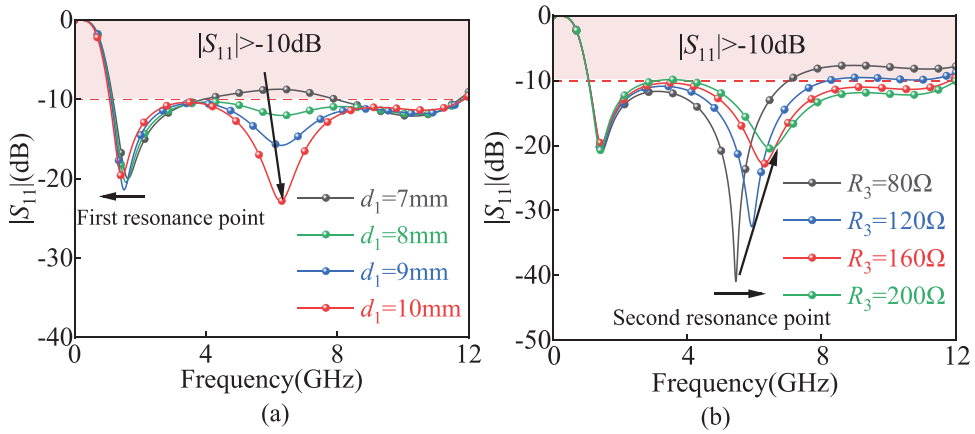

Figure 7. $|S_{11}|$ curves for different values of (a) d_1 and (b) R_3.

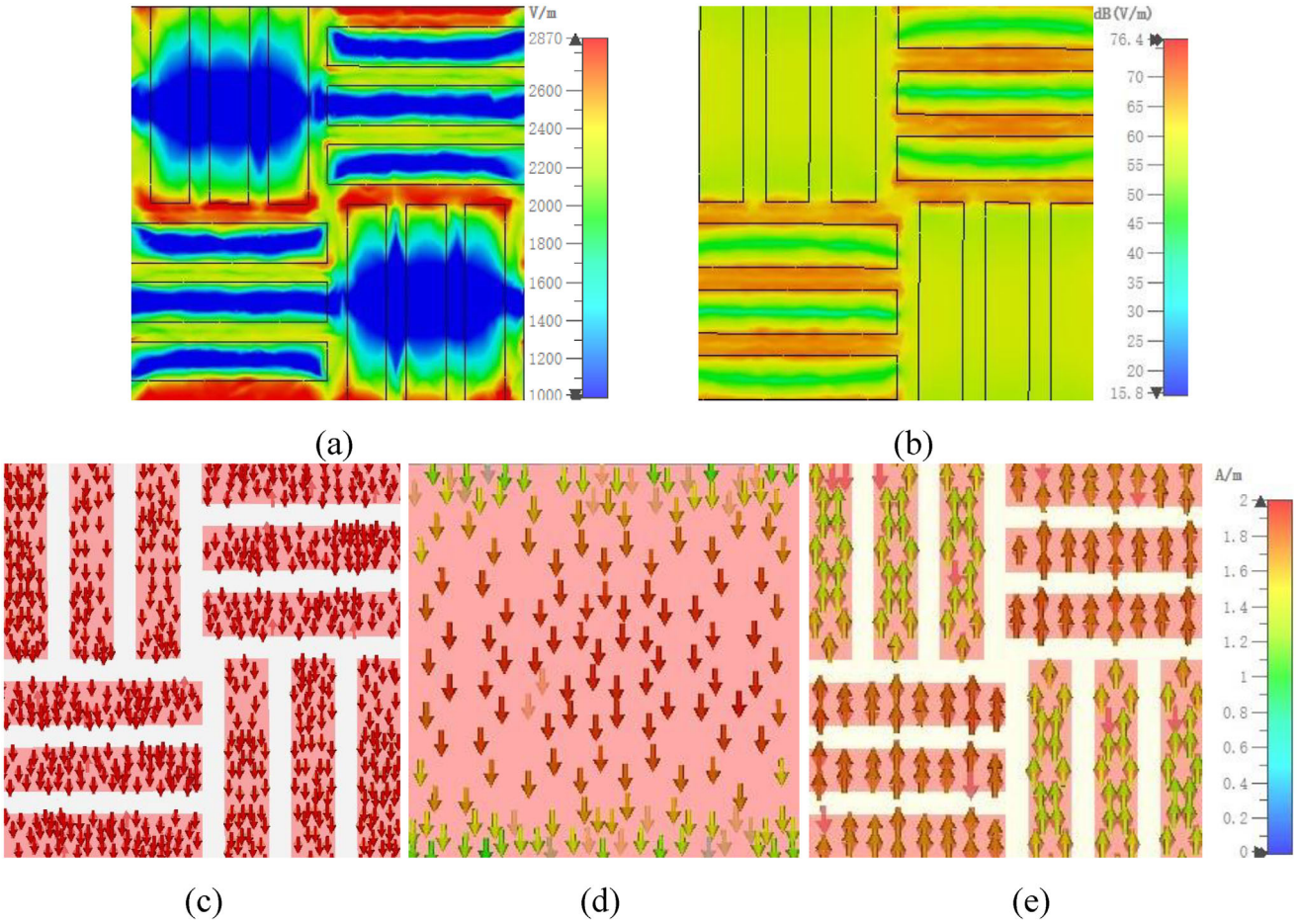

Figure 8. Electromagnetic responses of the proposed absorber under normal incident waves at 1.45 GHz. a) and (b) show the electric field distribution, and magnetic field distribution, respectively. c–e) show the surface current relationships among the surface resistive film layers in Config-1, Config-2, Config-3, and the copper grounded plane, respectively.

$$r = \left(\frac{l \cdot d_R}{\pi}\right)^{1/2} \tag{8}$$

Here, μ_0 and μ_r denote the vacuum permeability and the relative permeability, respectively. r denotes the effective radius based on the same cross-sectional area through which the current flows. l denotes the length of the current line. Together, these parameters determine the value of inductance. Each *RLC* component parameter is obtained through the derivation of equations for structural dimensions, resistivity, and capacitive coupling length, which establishes a clear relationship with the specific resistive film shape, dielectric thickness, and other physical parameters, thus providing good interpretability and predictability.

From above equations, the values for the equivalent *RLC* components were calculated as follows: $R_1 =$ 666.67 Ω, $R_2 =$ 212.56 Ω, $R_3 =$ 266.67 Ω, $C_1 = C_3 =$ 46.48 fF, $C_2 =$ 408 fF, $L_1 = L_3 =$ 46.48 nH. The *RLC* model consisting of these components allows each resonant unit to form a synergistic absorption in different frequency bands, especially in the fringe bands, where the superposition of the responses of multiple *RLC* units improves the impedance continuity and thus maintains a good absorption performance and weakens the rebound of reflectance.

2.3. Full-wave Simulation and Equivalent Circuit Results

To verify the correctness of the calculated values of the ECM, ADS software was employed to optimize the $|S_{11}|$ curve of ECM. It can be observed from **Figure 4** that the $|S_{11}|$ curve derived from the *RLC* model is generally slightly higher than the CST simulation curve within the operating band frequency band of 1–12 GHz, whereas it is slightly lower near the edges of the frequency band, and the resonance points obtained by ADS calculations are basically consistent with the resonance points of the full-wave simulation, which indicates that the *RLC* equivalent circuit model captures the absorber's broadband behavior well.

The comparison of theoretical and optimized values of *RLC* is presented in **Table 1**. It can be seen that there is high consistency between the theoretical and optimized values, indicating the accuracy of the proposed ECM. However, it should be noted that there are some discrepancies between the theoretical and

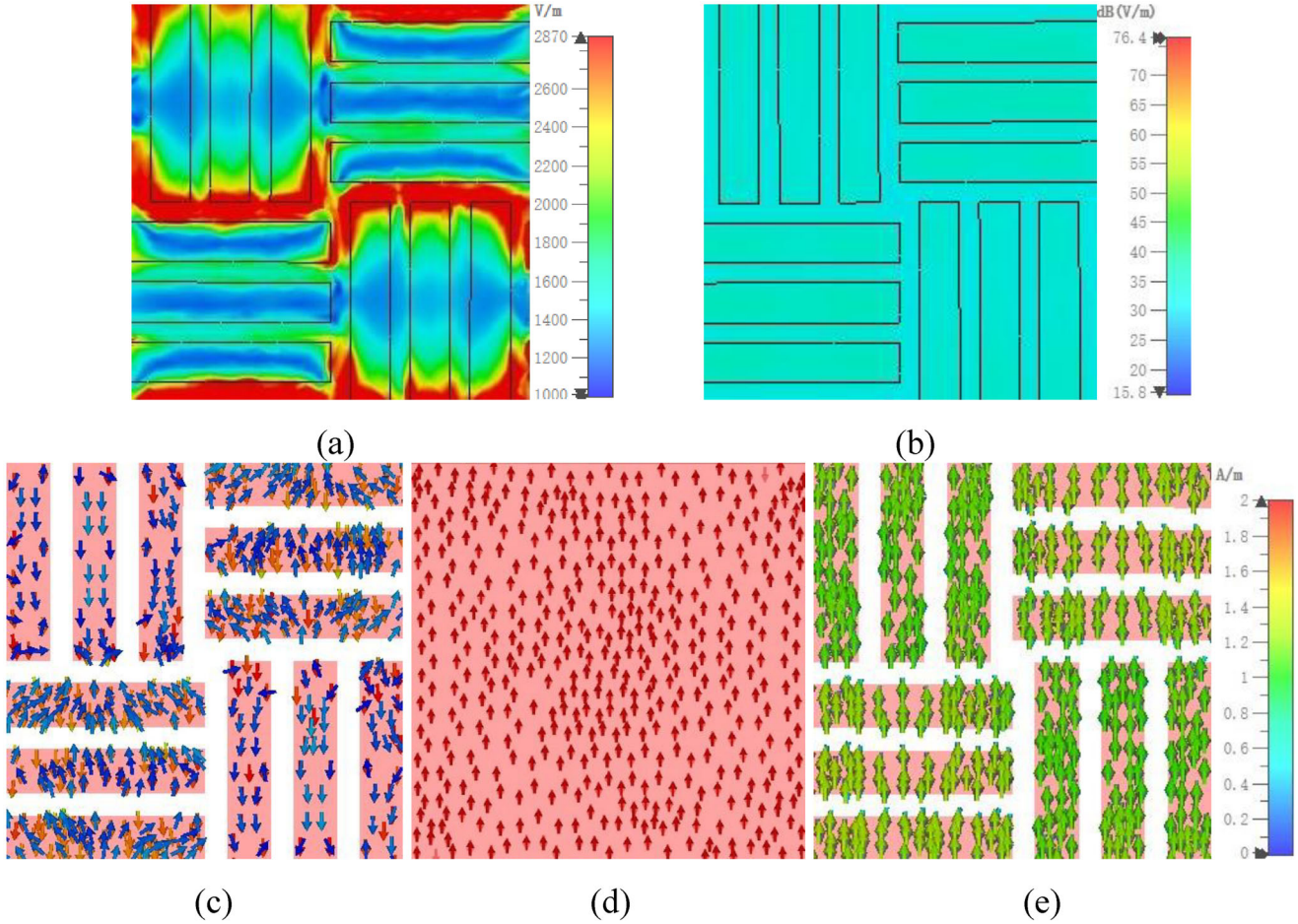

Figure 9. Electromagnetic responses of the proposed absorber under normal incident waves at 6.3 GHz. a) and (b) show the electric field distribution, and magnetic field distribution, respectively. c–e) show the surface current relationships among the surface resistive film layers in Config-1, Config-2, Config-3, and the copper grounded plane, respectively.

optimized values for the equivalent capacitance C_2 and C_3. This may be attributed to the complexity of the electromagnetic environment, leading to significant coupling between RFSS layers and affecting the equivalent capacitance.

The full-wave simulation $|S_{11}|$ curve has two distinct resonance points as well as a smoother resonance point, as shown in Figure 4. Analyzed for the absorption bands 1–12 GHz, the influence of resonance points generated by different layers on the absorption characteristics was discussed. With only RFSS1, the absorption curve generates the first resonance point at 4.9 GHz, but the absorption performance is poor. Typically, the absorption performance of a single-layer absorber is limited. By adding the RFSS2 layer, two resonance points at 1.7 and 9.7 GHz are introduced, and it can achieve more than 90% absorption in certain frequency band. However, it is not able to maintain high absorption in a continuous frequency band. After the RFSS3 layer added, a third resonance point appears, which further broadens the absorption bandwidth. Absorption performance of absorbers with different layer configurations are shown in **Figure 5**. The introduction of multiple resonant points through the superposition of multi-layer structure can achieve broadband absorption. However, there is a trade-off between achieving broadband absorption and minimizing thickness, leading to the selection of a three-layer structure. Moreover, the resistive film FSS structure improves impedance matching and effectively enhances absorption at different frequencies. Therefore, the combination of the resistive film FSS and the multi-layer structure introducing resonant points achieves ultra-broadband absorption.

3. Absorption Characterization

3.1. Multi-Angle Absorption Analysis

The polarization sensitivity and stability of oblique incidence is crucial for studying absorbers and serves as an important criterion for evaluating their effectiveness. **Figure 6a** shows the simulated $|S_{11}|$ curves at different angles of polarization. It is obvious to see that the change of polarization angle has almost no effect on the $|S_{11}|$ curve, so the absorber has polarization insensitivity. Figure 6b shows the simulated $|S_{11}|$ curves at different incidence angles for TE and TM modes. In TE mode, the reflection loss of the absorber gradually decreases as the incidence angle increases from 0° to 55°. Meanwhile, the $|S_{11}|$ remains

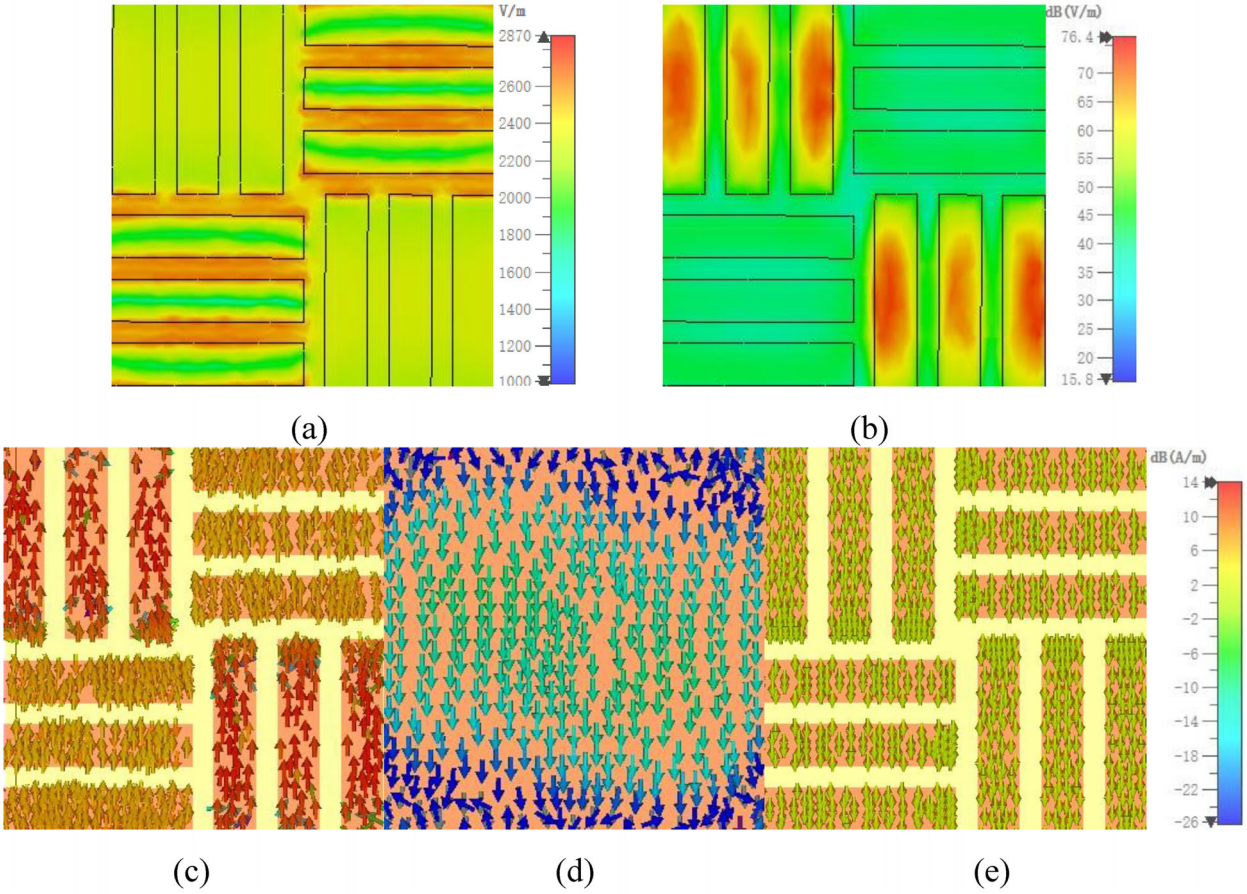

Figure 10. Electromagnetic responses of the proposed absorber under normal incident waves at 10.74 GHz. a) and (b) show the electric field distribution, and magnetic field distribution, respectively. c–e) show the surface current relationships among the surface resistive film layers in Config-1, Config-2, Config-3, and the copper grounded plane, respectively.

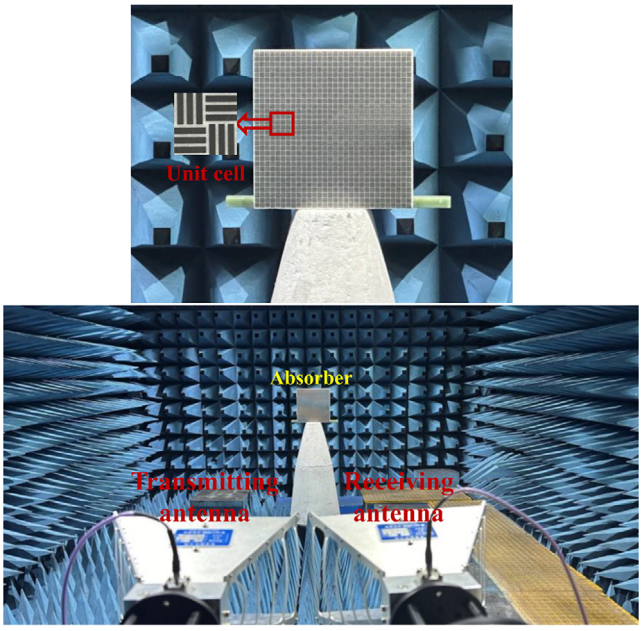

Figure 11. Measurement environment and the fabricated sample of MMA.

approximately below the −7 dB (i.e., 80% absorption). As the incidence angle increases, the absorption in TM mode outperforms that in TE mode.[23] Figure 6c shows that the $|S_{11}|$ remains below −10 dB within the 60° incidence angle. However, the absorption bandwidth of the absorber increases notably with changes in the angle in contrast to the TE mode. In summary, the proposed MMA demonstrates excellent stability and insensitivity up to 75° (absorption > 50%).

3.2. Parameter Analysis

The impact of the resistive film's resistance and size was explored based on the simulation and circuit analysis results. These factors affect the absorption of electromagnetic energy. The key structural parameters length d_1 of the single-strip resistive film and resistive film resistance R_3 was analyzed.

From **Figure 7a**, it can be seen that the first resonance point of the curve shifts to lower frequencies while the second resonance point shows deeper absorption as d_1 increases. The resonance tendency can be explained by $f = 1/2\pi\sqrt{LC}$,[24–26] combined with Equations (5–8). The values of inductance L and capacitance C increase with d_1 increasing, leading to the first

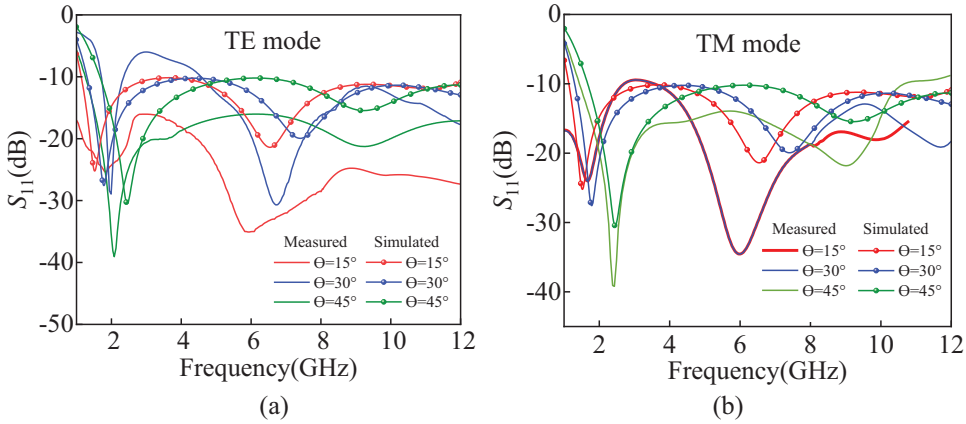

Figure 12. Comparison results of the measured and simulated $|S_{11}|$ curves at different incidence angles in (a) TE and (b) TM modes.

resonance point shifting to lower frequencies. For the second resonance point, the depth of the $|S_{11}|$ curve increases as the values of L and C increase, due to the strengthening of energy storage and dissipation. Overall, the optimal value of d_1 is determined to be 10 mm.

To clearly show the RFSS layer's ability to effectively absorb electromagnetic energy, Figure 7b presents the $|S_{11}|$ simulation curves for different values of R_3. From the Equations (2) and (4), the equivalent resistance R and the impedance Z_{RFSS} increase as R_3 increase. The system becomes more resistive as R increases, causing the resonance frequency to shift to higher frequencies. This is due to the increased resistance dampens the resonance, lowering the Q-factor and broadening the resonance. Additionally, the increased energy dissipation reduces the resonance depth. Consequently, the optimal value of R_3 is determined to be 160 Ω sq^{-1}.

3.3. Absorption Mechanism of the MMA

To provide a better understanding of the absorption mechanism of the overall structure, the electric field, the magnetic field, and surface current distribution at the resonance peeks of 1.45, 6.3, and 10.74 GHz were explored, as shown in **Figures 8, 9**, and **10**, respectively.

The electromagnetic responses under normal incident waves at 1.45 GHz resonance frequency are shown in Figure 8. From Figure 8a, the electric field is primarily centered around each resistive film frequency selective surface, indicating that an equivalent capacitance(C) is formed between the adjacent cells. Similarly, the magnetic field is primarily dispersed inside each resistive film, as shown in Figure 8b, indicating that the resistive film could be regarded as an equivalent inductor(L). From Figure 8c–e, the surface current distribution of each configuration layers combines with the copper grounded plane. For Config-1 (in Figure 1), each resistive film layer produces an opposite current to the copper grounded plane, which cause strong magnetic resonance. However, the Config-2 and Config-3 (in Figure 1) have the same direction, which strengthens the electrical resonance.

From Figure 9, the electric field, and magnetic field distributions at the frequency resonance point of 6.3 GHz are similar to those at 1.45 GHz. The difference is that part of Config-1 and Config-3, each resistive film layer produces the same current to the copper grounded plane, which strengthens the electrical resonance. In contrast, in Config-2 and the other part of Config-1, the currents flow in opposite directions, resulting in strong magnetic resonance.

From Figure 10, at the resonance frequency of 10.74 GHz, the magnitude of its electric and magnetic field strengths is smaller compared to the previous two resonance points, resulting in a lower absorption rate at this frequency. The current distribution is exactly the same as that at the resonance point of 1.45 GHz. In summary, the electric and magnetic resonances generated by different layers collectively enhance the absorption effectiveness at the high-frequency resonance point. This synergistic effect not only improves overall absorption performance but also contributes to achieving broadband absorption and effective electromagnetic shielding. By leveraging multiple resonant mechanisms, the structure ensures better impedance matching and energy dissipation, ultimately leading to a more efficient and wideband absorber.

4. Experimental Verification

To validate the correctness of the simulated results of the proposed MMA (300 × 300 mm surface area), the design was fabricated and the reflection coefficient was measured. The measurement environment and the processed sample to be tested are shown in **Figure 11**. The measured results conducted by a pair of standard wideband horn antennas working in 1–18 GHz, which are used as the transmitting and receiving devices. The VNA used in the experiment is Keysight E5063A, which has a a maximum measurement frequency of 18 GHz, a dynamic range of greater than 117 dB, a trace noise as low as 0.015 dB, and the fastest 201-point scan time of ≈9 ms. The two horn antennas are connected to the two ports of the VNA, respectively, and the sample is placed at a distance of ≈3 m from the antennas(The calculated distance that satisfies the far-field condition is 2.857 m).

Figure 12a,b show the sample's measured and simulated $|S_{11}|$ curves at different incidence angles in TE and TM modes, respectively. On the surface of the test results, the reflection coefficient < −8 dB (i.e., absorption >80%) can be achieved within incidence

Table 2. Performance comparison of some broadband microwave absorbers.

Refs.	Bandwidth [GHz]	Relative thickness [λ_L]	Thickness [mm]	FBW [≥90%]	Polarization insensitivity	Angular stability [>80%]
[27]	2.79–20.62	0.115	12.35	152	Yes	60°
[28]	1.64–18.52	0.143	26.1	167	Yes	45°
[29]	7.6–24.5	0.119	15.2	105	Yes	50°
[30]	3.6–24.6	0.15	12.5	149	Yes	50°
Our work	1.07–11.84	0.105	29.525	166	Yes	55°

angles up to 30° in both TE and TM modes. Additionally, even at an angle of incidence of 45°, the reflection coefficient is below −7 dB, and the absorber maintains an absorption of more than 70%. The magnetic field strength decreases as the incidence angle increases in TE mode. Additionally, the electric field strength also decreases with the increasing incidence angle in TM mode, but the absorption performance is less affected by changes in the electric field strength. In a word, the absorber maintains greater than 70% absorption at incidence angles within 45° in both TE and TM modes, providing an excellent wide-angle absorption performance. The measured results basically consist with the resonance points of the simulation results, and the errors are mainly in the absorption depth. The discrepancies between experimental and simulation results are attributed to factors such as the uneven resistance value of the processed resistive film which is most likely caused by uneven paste or target material, unstable spinning speed during screen printing and the influence of ambient temperature and humidity, and the finite size of the sample as well as the noise interference in the laboratory, however, the measured results are in agreement with the simulated results to a large extent.

Table 2 summarizes the performance comparison of existing broadband microwave absorbers. It is seen that the ref. [27] proposed the absorber with good angular stability, but their fractional bandwidth and low-frequency absorption capabilities are inferior. refs. [28–30] proposed with thinner overall structures compared to our work. However, our work performs better in fractional bandwidth, low-frequency absorption, and angular stability, making it more suitable for broadband applications. In conclusion, our work achieves an excellent balance between ultra-wideband absorption, low-frequency absorption, and angular stability. This provides significant advantages over most existing designs, making it well-suited for applications in stealth technology and other related fields.

5. Conclusion

In this paper, an ultra-broadband metamaterial absorber based on multilayer resistive film frequency selective surface is proposed. Full-wave simulation and measurement were carried out for validation of the structure. The experimental results present that the metamaterial absorber (MMA) achieves a −10 dB bandwidth ranging from 1.07–11.84 GHz at normal incidence. The absorption range of the proposed MMA almost covers the *L*-, *S*-, *C*-, and *X*-bands. Moreover, the fractional bandwidth of the absorber is 166% and its thickness is only 0.105 λ_L. The absorption rate remains above 80% for both TE and TM polarizations within 55° incidence angles. Moreover, the measured results of the absorber agree well with the simulated ones, indicating that the proposed structure can be widely used in stealth technology and other related fields.

Acknowledgements

The authors wish to thank all reviewers for their valuable suggestions. This work was supported by the Natural Science Foundation of Jiangsu Province under Grant No. BK20221115; the National Natural Science Foundation of China under Grant No. 62371451.

Conflict of Interest

The authors declare no conflict of interest.

Data Availability Statement

Data sharing is not applicable to this article as no new data were created or analyzed in this study.

Keywords

metamaterial absorber (MMA), resistive frequency selective surface (RFSS), RLC circuit

Received: April 11, 2025
Revised: June 11, 2025
Published online: July 1, 2025

[1] H. Lv, Z. Yang, H. Pan, R. Wu, *Prog. Mater. Sci.* **2022**, *18*, 100946.
[2] S. Narayan, J. Sreeja, V. V. Surya, B. Sangeetha, R. U. Nair, *J. Electron. Mater.* **2020**, *49*, 1728.
[3] J. Song, C. Huang, J. Yang, X. Zhang, J. Peng, X. Luo, *IEEE Trans. Antennas Propag.* **2020**, *68*, 2446.
[4] K. Deng, F. Li, X. Wang, J. Feng, C. Xu, *Mater. Res. Express* **2024**, *11*, 025801.
[5] J. B. Kim, J. H. Byun, *IEEE Trans. Electromagn. Compat.* **2012**, *54*, 37.
[6] J. Reinert, J. Psilopoulos, J. Grubert, A. F. Jacob, *Microwave Opt. Technol. Lett.* **2001**, *30*, 254.
[7] T. Jang, H. Youn, Y. J. Shin, L. Jay Guo, *ACS Photonics* **2014**, *1*, 279.
[8] E. F. Knott, C. D. Lunden, *IEEE Trans. Antennas Propag.* **1995**, *43*, 1339.
[9] S. Ji, H. Ren, C. Zhang, J. Zhao, H. Wu, H. Dai, *J. Phys. D-Appl. Phys.* **2023**, *56*, 425101.
[10] J. Dong, Y. Ma, M. Wang, *IEEE Antennas Wirel. Propag. Lett.* **2023**, *22*, 2970.

[11] Y. Li, P.-F. Gu, Z. He, Z. Cao, J. Cao, K. W. Leung, *IEEE Trans. Antennas Propag.* **2022**, *70*, 11911.
[12] Z. Yao, S. Xiao, Y. Li, B. Z. Wang, *IEEE Trans. Antennas Propag.* **2022**, *70*, 7276.
[13] Z. Hao Wen Lan, M. Li, X. L. Weng, L. Qi, K. Li, R. Zhang, X. Zhou, Y. Wu, M. Bi, *Appl. Opt.* **2023**, *62*, 1096.
[14] J. Zheng, H. Zheng, Y. Pang, B. Qu, Z. Xu, *Opt. Express.* **2023**, *31*, 3731.
[15] H. Li, H. Dong, Y. Zhang, N. Mou, Y. Xin, R. Deng, L. Zhang, *Opt. Express* **2021**, *29*, 18446.
[16] F. Costa, S. Genovesi, A. Monorchio, G. Manara, *IEEE Trans. Antennas Propag.* **2013**, *61*, 1201.
[17] Y. Han, W. Q. Che, C. Christopoulos, Y. M. Chang, *IEEE Trans. Electromagn. Compat.* **2015**, *57*, 22.
[18] F. Gronwald, J. Nitsch, S. Tkachenko, *Electr. Engineer.* **2011**, *93*, 147.
[19] X. Kong, S. Zhang, X. Pang, Y. Fu, L. Zhao, Z. Shen, *IEEE Antennas Wirel. Propag. Lett.* **2024**, *23*, 1869.
[20] Y. Li, D. Li, H. Luo, F. Chen, X. Wang, R. Gong, *IEEE Trans. Antennas Propag.* **2018**, *66*, 6057.
[21] D. Li, J. Yang, X. Wang, T. Wang, R. Gong, *IEEE Trans. Microwave Theor. Techn.* **2022**, *70*, 232.
[22] F. Costa, A. Monorchio, G. Manara, *IEEE Antennas Propag. Mag.* **2012**, *54*, 35.
[23] J. Zheng, H. Zheng, Y. Pang, B. Qu, Z. Xu, *Opt. Express* **2023**, *31*, 3731.
[24] L. Zhang, P. Zhou, H. Chen, H. Lu, J. Xie, L. Deng, *Appl. Phys. A-Mater. Sci. Process.* **2015**, *121*, 233.
[25] H. B. Zhang, L. W. Deng, P. H. Zhou, L. Zhang, D. M. Cheng, H. Y. Chen, D. F. Liang, L. J. Deng, *J. Appl. Phys.* **2013**, *113*, 013903.
[26] P. Chen, X. Kong, J. Han, W. Wang, K. Han, H. Ma, L. Zhao, X. Shen, *Chin. Phys. Lett.* **2021**, *38*, 027801.
[27] Z. Sun, L. Yan, X. Zhao, R. X.-K. Gao, *IEEE Antennas Wirel. Propag. Lett.* **2023**, *22*, 789.
[28] N. Wang, G. Wan, Q. Ding, X. Ma, *IEEE Antennas Wirel. Propag. Lett.* **2024**.
[29] C. Liang, X. Kong, F. Wang, R. Xu, Y. Fu, X. Pang, L. Zhao, *J. Electromagn. Waves Appl.* **2022**, *37*, 401.
[30] V. P. Inbavalli, V. P. Sakthivel, C. Venkatesh, S. Kumar T R, *IEEE Trans. Electromagn. Compat.* **2023**, *65*, 2065.